Mon. Not. R. Astron. Soc. **370,** 1797–1803 (2006) doi:10.1111/j.1365-2966.2006.10590.x

Reconciling optical and X-ray mass estimates: the case of the elliptical galaxy NGC 3379

Silvia Pellegrini and Luca Ciotti★

Astronomy Department, University of Bologna, via Ranzani 1, 40127 Bologna, Italy

Accepted 2006 May 19. Received 2006 May 18; in original form 2006 March 24

ABSTRACT

NGC 3379 is a well-studied nearby elliptical for which optical investigations have claimed a little dark matter content, or even no dark matter. Recently, its total mass profile $M(r)$ has been derived by exploiting *Chandra* observations of its extended and X-ray emitting interstellar medium, based on the hypothesis of hydrostatic equilibrium for the hot gas. The resulting total mass within the effective radius R_e has been claimed to be a few times larger than that found by optical studies. Here, we show that part of the discrepancy can be due to an underestimate of the optically derived mass, and the remaining discrepancy of a factor of $\sim$2 can be explained by deviations from hydrostatic equilibrium of the hot gas. By using hydrodynamical simulations tailored to reproduce the observed hot gas properties of NGC 3379, and by assuming as input for the simulations the total mass profile derived optically, we show that (i) the hot gas at the present time has X-ray properties consistent with those observed only if it is outflowing over most of the galactic body, and (ii) an overestimate of M of the same size found in the recent X-ray analysis is recovered when assuming hydrostatic equilibrium. We also show that the hot gas is outflowing even for a dark matter fraction within R_e as large as derived with the standard X-ray procedure based on the hydrostatic equilibrium assumption, which shows the unapplicability of the method for this galaxy. Finally, we find that the whole range of dark mass amount and distribution allowed for by optical studies is compatible with a hot gas flow with the observed X-ray properties.

Key words: galaxies: elliptical and lenticular, cD – galaxies: individual: NGC 3379 – galaxies: kinematics and dynamics – galaxies: structure – X-rays: galaxies – X-rays: ISM.

1 INTRODUCTION

The presence of an extended and X-ray emitting interstellar medium (ISM) in early-type galaxies has been often used as a tool to determine their dynamical properties, in particular their mass profile and total mass out to large radii ($\sim$10 optical effective radii R_e; e.g. Fabbiano 1989). Most recently, this kind of analysis has been performed for a sample of 53 early-type galaxies by exploiting *Chandra* data (Fukazawa et al. 2006, hereafter F06). In the commonly adopted approach, a spherical mass distribution is assumed and, in the hypothesis of hydrostatic equilibrium, the total mass profile is recovered via the well-known formula (Fabricant, Lecar & Gorenstein 1980):

$$M(r) = -\frac{kTr}{G\mu m_p}\left(\frac{\mathrm{d}\log\rho}{\mathrm{d}\log r} + \frac{\mathrm{d}\log T}{\mathrm{d}\log r}\right), \quad (1)$$

where T and ρ are the radial temperature and density profiles, inferred from deprojection techniques (e.g. White, Jones & Forman 1997), m_p is the proton mass, μ is the mean molecular weight and k is the Boltzmann constant. Using equation (1), several authors measured the total mass of X-ray bright, nearby early-type galaxies, finding in general larger masses than obtained with optical studies (e.g. Ciotti & Pellegrini 2004 and references therein, hereafter CP04), or sometimes lower than these, in the central galactic regions (Tsai 1994). In fact, mass profiles can be derived also from the observed stellar velocity dispersion profiles $\sigma_p(R)$; these extend out to $\sim$1–2 R_e in few best cases (e.g. Bertin et al. 1994; Kronawitter et al. 2000). For example, by solving the Jeans equations for assumed visible and dark density profiles and a specified radial trend of anisotropy in the stellar velocity dispersion tensor, one obtains $\sigma_p(R)$ to be compared with the observed one. This method suffers from a 'dark matter–anisotropy degeneracy', because radial orbital anisotropy can mimic the presence of a massive dark matter halo (e.g. Tonry 1983). This technique has also been used considering as tracers planetary nebulae or globular clusters (Romanowsky et al. 2003; Teodorescu et al. 2005; Pierce et al. 2006), giving a variety of results. However, optical studies converge towards an amount of dark mass that is less than the optical mass within R_e (or even much lower, see Cappellari et al. 2006 for the most recent analysis

★E-mail: luca.ciotti@unibo.it

Table 1. General and hot ISM properties of NGC 3379.

D (Mpc)	Morphological type	B_0^T (Bmag)	L_B ($10^{10}\,L_{B,\odot}$)	$R_e{}^a$ ($''$, kpc)	$\sigma_c{}^b$ (km s^{-1})	$L_X{}^c$ (erg s^{-1})	Band (keV)	kT^c (keV)
10.6	E1	10.18	1.5	37.5, 1.93	221	4.6×10^{37}	0.2–5	0.52 ± 0.30

Notes. D is from Tonry et al. (2001); the morphological type and B_0^T are from RC3; L_B derives from B_0^T and the adopted distance.
[a]Peletier et al. (1990). [b]Central stellar velocity dispersion from Halliday et al. (2001). [c]Fukazawa et al. (2006).

based on SAURON data), and possibly larger outside. The use of the hot ISM to derive dynamical quantities using equation (1) is then appealing both for its capability to reach large radii and for being exempted from the orbital anisotropy degeneracy problem.

In a recent work, however, the accuracy of the X-ray based estimates of the total mass with equation (1) [hereafter $M^{\rm X}_{\rm est}(r)$] has been questioned (CP04). Instead of equation (1), a more general expression for the momentum equation of the hot ISM is (e.g. Ciotti et al. 1991):

$$\frac{k}{\mu m_{\rm p}\rho}\frac{{\rm d}\rho T}{{\rm d}r} + \mathcal{V} = -g, \tag{2}$$

where $g = GM(r)/r^2$ describes the total gravitational field and $\mathcal{V}$ is the kinetic term that includes all the non-hydrostatic contributions, such as the time dependence of the velocity, the advective term and the presence of mass sources. CP04 investigated the effect that deviations from hydrostatic equilibrium have on $M^{\rm X}_{\rm est}(r)$ derived via equation (1), and showed that

$$M^{\rm X}_{\rm est} = M + \frac{r^2}{G}\mathcal{V}. \tag{3}$$

They found that less-massive distributions than true are deduced for the central regions of galaxies hosting inflowing gas, and conversely that the true mass is overestimated for outflowing regions where the velocity increases with radius, as in galactic winds.

Currently, quite accurate T and ρ profiles are being derived from *Chandra* and *XMM–Newton* observations (e.g. Sun et al. 2003; F06). F06, in particular, investigated the dynamical structure of 53 elliptical galaxies, both X-ray bright and X-ray faint; by exploiting the high angular resolution of *Chandra*, they obtained a temperature and density profile from 0.1 to $10R_e$. For the well-studied nearby elliptical NGC 3379, they derived an $M^{\rm X}_{\rm est}$ of approximately seven times the value obtained with optical methods, for the same galactic region. Here, we demonstrate how deviations from hydrostatic equilibrium can be responsible for the discrepancy between $M^{\rm X}_{\rm est}$ and the mass estimated from optical studies, for this galaxy. By using hydrodynamical simulations tailored to reproduce the hot gas properties observed by *Chandra* for NGC 3379, it is shown that an overestimate is obtained from the use of equation (1), since the hot ISM is largely outflowing. In Section 2, we briefly describe the previous mass estimates for NGC 3379 coming from optical studies and from the recent X-ray analysis; in Section 3, we present the galaxy model used for the hydrodynamical simulations and the results of the simulations; in Section 4, the conclusions are presented.

2 THE TOTAL MASS PROFILE OF NGC 3379

NGC 3379 is the dominant elliptical galaxy in the nearby Leo Group, and has an optical profile well described by a de Vaucouleurs (1948) law over a span of 10 magnitudes (Capaccioli et al. 1990; see Table 1 for the main galaxy properties). Its optical shape is roundish (its morphological type is E1) and its optical colours are typical of an old population; it shows no sign of current or past interactions (Schweizer & Seitzer 1992). The total mass profile of NGC 3379 has been studied several times using optical data (hereafter, all quantities involving distance have been rescaled for the distance in Table 1; M indicates the total mass, M_* the stellar mass and $M_{\rm h}$ the dark halo mass).

2.1 Results of optical studies

Even when performed with different approaches, optical studies invariably show very little dark matter within R_e. Their results are usually expressed in terms of the B-band total mass-to-light ratio M/L_B. For NGC 3379, the contribution of M_*/L_B to the total M/L_B has been estimated to range from 4.2 to 8.8 from stellar population synthesis models (Gerhard et al. 2001).

The dynamical modelling by Saglia, Bertin & Stiavelli (1992), based on kinematical data extending out to $\sim 1.7R_e$, gives a best-fitting $M/L_B = 7.8$ for a one-component modelling, for the whole galaxy. In their phase-space-based two-component modelling, they found $M_*/L_B = 7.5$, and a dark-to-luminous mass ratio $M_{\rm h}/M_* = 0.67^{+0.16}_{-0.30}$ within R_e, and $M_{\rm h}/M_* = 1.4^{+3.6}_{-0.7}$ for the whole galaxy.

Kronawitter et al.'s (2000) dynamical modelling, based on stellar kinematic information including line profile, and extending from 0.005 to $2.75R_e$, shows an outward increase of M/L_B of a factor of $1.2^{+0.4}_{-0.2}$, with respect to a central value of $M/L_B = 5.6^{+0.25}_{-0.37}$ (though the modelling is also consistent with a flat M/L_B over the range of the kinematic data). At R_e, they gave[1] $M/L_B = 6.3$, which implies $M_{\rm h}/M_* = 0.13$ when for M_*/L_B the central M/L_B is adopted. At their outermost data point, $M_{\rm h}/M_* = 0.2^{+0.4}_{-0.2}$.

More recent modelling of long-slit data extending to 80 arcsec found again that dark matter is not required out to $\sim 2.1R_e$ (Samurovic & Danziger 2005); the data can be fitted with a constant $M/L_B = 6$–11. SAURON observations of the central region of NGC 3379 give integral-field stellar kinematics out to 28 arcsec (Cappellari et al. 2006). Coupled with two-integral Jeans and three-integral Schwarzschild dynamical models, the data are consistent with a constant mass-to-light ratio in the I band; from their M_*/L_I for the stellar population, $M_{\rm h}/M_* \sim 0.09$ is recovered.

The mass profile has been studied also at larger radial distances using planetary nebulae as tracers. Ciardullo, Jacoby & Dejonghe (1993) presented a radial velocity survey of planetary nebulae with galactocentric radii $\lesssim 4.5R_e$. At large radii, the stellar dispersion profile joins with that of the planetary nebulae. The velocity dispersion and photometric profiles agree with a constant mass-to-light ratio isotropic orbit model with $M/L_B \sim 7$, similar to what is obtained with anisotropic models; therefore, it was concluded that dark matter is not needed within $\sim 4.5R_e$.

[1] This is a ratio between spatial quantities, that is, between the mass and luminosity enclosed within a sphere of radius $r = R_e$ (Saglia, private communication).

Romanowsky et al. (2003) found a decrease in the velocity dispersion profile of planetary nebulae extending out to 200 arcsec. Within this radius, their modelling constrained $M/L_B = 7.1 \pm 0.6$, a result consistent with no dark matter, given the possible M_*/L_B values (Gerhard et al. 2001). Dekel et al. (2005) questioned this result with radially anisotropic modelling, and showed that a total $M/L_B \sim 15$ at $5R_e$ is consistent with the data; this implies $M_h/M_* =$ 1.1–1.5 (for an assumed $M_*/L_B = 6$–7).

Summarizing, the optical studies converge towards a very small dark matter content within R_e, of the order of $M_h/M_* \sim 0.1$, except for Saglia et al.'s (1992) analysis that gives $M_h/M_* = 0.37$–0.83. At larger radii, the dynamical modelling gives results consistent with no dark matter, but also with a global galactic value of $M_h/M_* =$ 1.1–1.5 (Dekel et al. 2005) or even $M_h/M_* = 0.7$–5 (Saglia et al. 1992).

2.2 Results of X-ray studies and first reduction of the discrepancy

The hot gas content of NGC 3379 is very low, as known since *ROSAT* observations (e.g. Trinchieri et al. 2000; Brown & Bregman 2001; Pellegrini 2005). The most recent *Chandra* data had been used by F06 to derive the total mass within R_e. From a parametrized gas density and temperature profile entered in equation (1), F06 obtained $M^X_{est} = 8.7 \times 10^{10}\,M_\odot$, with a quoted 'typical error' of 30 per cent [therefore $M^X_{est} = (8.7 \pm 2.6) \times 10^{10}\,M_\odot$]. From within the same region, we derive a total $M = 3.7 \times 10^{10}\,M_\odot$, by taking M/L_B at R_e of Kronawitter et al. (2000) (see Section 2.1) and[2] 0.42× their quoted L_B. Therefore, we determine a discrepancy of a factor of ∼2 between the X-ray and the optical estimate.

F06 noted a larger discrepancy with the mass derived by Kronawitter et al. (2000), by a factor of ∼7 (see their table 5); however, they likely underestimated Kronawitter et al.'s total mass within R_e, for which they gave just $1.3 \times 10^{10}\,M_\odot$. In fact, this mass cannot be smaller than $(M/L_B)_c \times 0.42 L_B = 3.3 \times 10^{10}\,M_\odot$, where $(M/L_B)_c = 5.6$ is the central mass-to-light ratio of Kronawitter et al. In any case, $M_*/L_B > 4$ for the old stellar population of NGC 3379 (Gerhard et al. 2001), which already implies $M_* > 2.5 \times 10^{10}\,M_\odot$ within $r = R_e$.

All in all, the observational results that will be considered in the following are that (i) M^X_{est} within R_e is a factor of ∼2 larger than the total mass estimated by Kronawitter et al. within the same radius; (ii) when taking an average $M_*/L_B \sim 6$ for the stellar population and the L_B value in Table 1, M^X_{est} corresponds to $M_h/M_* \sim 1.3$ within R_e.

In the next section, with the aid of hydrodynamical simulations, we show how an overestimate of a factor of 1.5–2 for the total mass of NGC 3379 can be easily obtained when using equation (1) instead of equation (2), since the hot gas is not in hydrostatic equilibrium, but instead it is outflowing over most of the galactic body. A summary of the hot gas properties derived by F06 is given in Table 1; even though resolved point sources have been subtracted before deriving these properties, some residual emission from unresolved stellar sources is still contributing to the X-ray luminosity of the gas in Table 1.

[2] For the de Vaucouleurs (1948) law, the luminosity enclosed within a spherical radius $r = R_e$ is ≃0.42 of the total one.

3 THE HYDRODYNAMICAL SIMULATIONS

The time-dependent equations of hydrodynamics with source terms, and the numerical code used to solve them, are fully described in Ciotti et al. (1991). The model galaxy is initially devoid of gas, a situation produced by the galactic winds established by Type II supernovae (SNe II), early in the evolution of elliptical galaxies. Then the mass losses from the evolving stellar population start replenishing the interstellar space, and the resulting gas flow evolution is followed until an age of ∼9 Gyr is reached, that is, the estimated age for NGC 3379 (Terlevich & Forbes 2002 gives an age of $9.0^{+2.3}_{-1.9}$ Gyr).

The X-ray luminosity in the energy band adopted by F06 has been calculated using the APEC code in XSPEC, for the density and temperature distribution of the gas given by the simulations (solar abundance has been adopted). The luminosity-weighted emission temperature in the same energy band has also been calculated for the models.

3.1 The galaxy model

A very good approximation of the de Vaucouleurs (1948) law is given by the Hernquist (1990) distribution, that has the advantage that all its dynamical properties can be expressed analytically. This distribution is

$$\rho(r) = \frac{M}{2\pi}\frac{r_c}{r(r_c + r)^3}, \tag{4}$$

where r_c is the scalelength and relates to the effective radius as $r_c \simeq R_e/1.8153$. This law gives a description of the luminous mass distribution accurate enough for the treatment of hot gas flows, on the scales that are relevant for the problem (from few tens to several thousands of parsecs). In the simulations, we adopt a central grid spacing of 5 pc to allow for a better sampling of the inner regions.

The radial density distribution of the dark haloes of ellipticals is not well constrained by observations; theoretical arguments favour a peaked profile (Ciotti & Pellegrini 1992; Evans & Collett 1997), and high-resolution numerical simulations of dissipationless collapse produce a density distribution $\propto r^{-1}$ near the centre (Dubinski & Carlberg 1991; Navarro, Frenk & White 1996). The model galaxy is therefore a superposition of two Hernquist density distributions, one for the luminous matter $\rho_*(r)$ with $r_c = r_*$ and $M = M_*$ in equation (4), and the other for the dark matter $\rho_h(r)$ with $M = M_h$, $r_c = r_h = \beta r_*$.

In order to build a galaxy model where the masses of the two components and their distributions are consistent with observations and also produce the observed σ_c, we solve and project the Jeans equations for a globally isotropic two-component Hernquist model. For this model, we find that a very accurate fit of the projected, mass-averaged stellar velocity dispersion within $R_e/8$ is

$$\sigma_c^2 \simeq \frac{GM_*}{r_*} \times \left(0.096 + 0.12\frac{M_h/M_*}{\beta^{1.72}}\right), \tag{5}$$

with

$$\beta = 2.8153\sqrt{\frac{M_h/M_*}{(M_h/M_*)_e}} - 1.8153, \tag{6}$$

where $(M_h/M_*)_e$ is the dark-to-luminous mass ratio within a radius $r = R_e$. Thus for assigned R_e, σ_c, total M_h/M_* and $(M_h/M_*)_e$, we derive M_* and β from equations (5) and (6). The typical stellar mass-to-light ratios resulting from this procedure, for $(M_h/M_*)_e = 0.1$–1,

are between 4 and 8. The model phase-space distribution function is everywhere positive (Ciotti 1996).

3.2 Time-evolving inputs

The time-evolving input ingredients of the numerical simulations are the rates of stellar mass loss from the ageing stellar population, and the rate of SN Ia heating. In the numerical code, the exact mass-return rate prescribed by the stellar-evolution theory is used (see e.g. Ciotti et al. 1991), updated to take into account the latest stellar population synthesis models (Maraston 2005) and more recent estimates for the mass ejection from stars as a function of their mass (Renzini & Ciotti 1993). The SN Ia heating rate is parametrized as $L_{\rm SN}(t) = E_{\rm SN} R_{\rm SN}(t) L_B$, where $E_{\rm SN} = 10^{51}$ erg is the kinetic energy injected in the ISM by one SN Ia, and the number of events as a function of time is $R_{\rm SN}(t)L_B \propto t^{-s}$, where the slope s describes the unknown decay rate (see also Pellegrini & Ciotti 1998). $R_{\rm SN}(t)$ is normalized to give the SN Ia explosion rate in nearby E/S0s for $t = 10$ Gyr, that is, $0.18h_{75}^2$ SNu (where 1 SNu = 1 SN Ia per 100 yr per $10^{10} L_{B,\odot}$, $h_{75} = H_0/75$), that has an associated uncertainty of ∼30 per cent (Cappellaro, Evans & Turatto 1999). Therefore, we consider as a free parameter also the ratio ϑ between the adopted SN Ia rate and the best-fitting estimate of Cappellaro et al., with $\vartheta = 0.67$–1.33. From a comparison between realistic modellings of the rate and its observation in high-z surveys currently available, a slope $s \sim 1.0$–1.2 has been favoured (Greggio 2005).

Another heating source, though less important than SNe Ia, is the thermalization of the stellar mass losses to the local 'temperature' set by the stellar velocity dispersion. At each radius, this is determined using the velocity dispersion profile obtained by solving the Jeans equation for the two-component Hernquist model in the globally isotropic case (Ciotti 1996). If anisotropy is present, this heating differs locally from the value it has in the isotropic case. However, the difference is small for realistic anisotropy distributions, and the total heating over the galaxy is independent of orbital anisotropy, as a consequence of the virial theorem. In addition, the heating due to thermalization of stellar motions is significantly smaller than SN Ia heating and, therefore, the effects of anisotropy on $M^{\rm X}_{\rm est}(r)$ are negligible [they are just indirect effects in equations (7)–(8) of the next section, through the gas temperature and velocity terms].

3.3 Results

In Section 3.3.1 below, we adopt the underlying total mass distribution on which most of the modelling of the optical data converges (Section 2.1). In Section 3.3.2, we use as input the mass model found by F06 and also a 'maximum' dark matter model. In both sections, we vary SN Ia parameters ϑ and s to obtain X-ray gas properties as observed when an age of ∼9 Gyr is reached. When this is the case, we apply to the radial distributions of the gas density and internal energy, resulting from the numerical simulation, the standard procedure of equation (1), in order to recover $M^{\rm X}_{\rm est}(r)$ and compare it with the true underlying mass distribution $M(r)$. In practice, we calculate the 'empirical' $M^{\rm X}_{\rm est}(r)/M(r)$ ratio from the output of the numerical simulations as

$$\frac{M^{\rm X}_{\rm est}(r)}{M(r)} = -\frac{k}{\mu m_{\rm p} \rho g}\frac{{\rm d}\rho T}{{\rm d}r}. \qquad (7)$$

This ratio is also given by equation (3), where the $\mathcal{V}$ term can be explicitly calculated from the momentum equation (see equation 10 of CP04)). In quasi-stationary conditions, as those reached by our models at the end of the simulations, one can neglect the $\partial u/\partial t$ term in the expression for $\mathcal{V}$, and the full expression for equation (3) becomes

$$\frac{M^{\rm X}_{\rm est}(r)}{M(r)} = 1 + \frac{u\dot{\rho}}{\rho g} + \frac{1}{2g}\frac{{\rm d}u^2}{{\rm d}r}, \qquad (8)$$

where $\dot{\rho}$ is the local mass injection rate due to stellar mass losses and u is the radial flow velocity. Equation (8) allows for a quantitative evaluation of the separate contributions of the non-hydrostatic terms to the $M^{\rm X}_{\rm est}(r)/M(r)$ ratio.

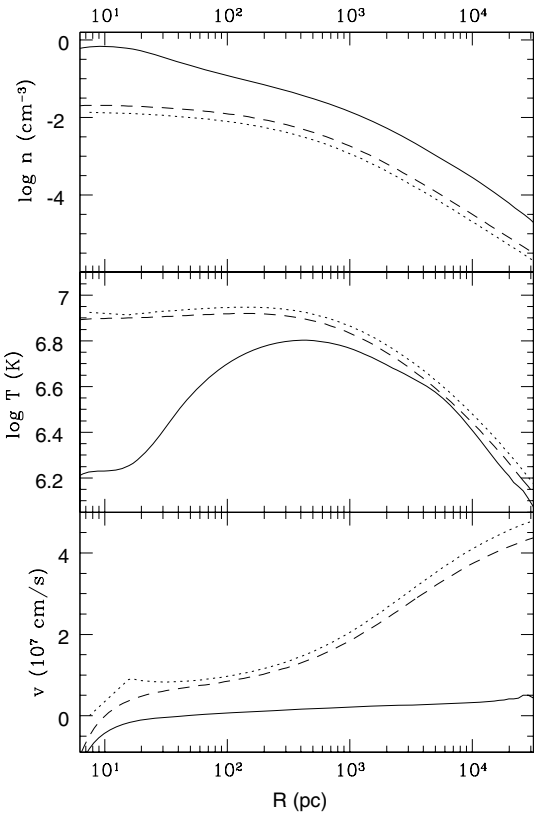

Figure 1. From the top to bottom panel, the radial profiles of the gas density, temperature and velocity for representative models of inflow (solid line), partial wind (dashed line) and global wind (dotted line) are shown; see Section 3.3.

By varying the input parameters, the resulting gas flow phases are of a global wind, a partial wind (where the gas is inflowing only over a very small central region) and a global inflow; a sample of the radial profiles of gas velocity, temperature and density for representative models of these three phases at the present epoch is shown in Fig. 1 (see Pellegrini & Ciotti 1998 for a more detailed description of the gas flow evolution).

3.3.1 Optically derived total mass model

In this experiment, the galaxy model is based on the conclusions of Section 2.1: it has $(M_{\rm h}/M_*)_{\rm e} = 0.13$, in accordance with Kronawitter et al. (2000), and a global $M_{\rm h}/M_* = 1.5$, consistent with the results of Dekel et al. (2005) and Saglia et al. (1992). The other parameters are set to the observed values given in Table 1.

With this total mass profile, the hot ISM maintains in a global wind phase throughout its evolution, if SN Ia rate is such that $\vartheta = 1$, regardless of the slope s. After a time equal to the age estimated for

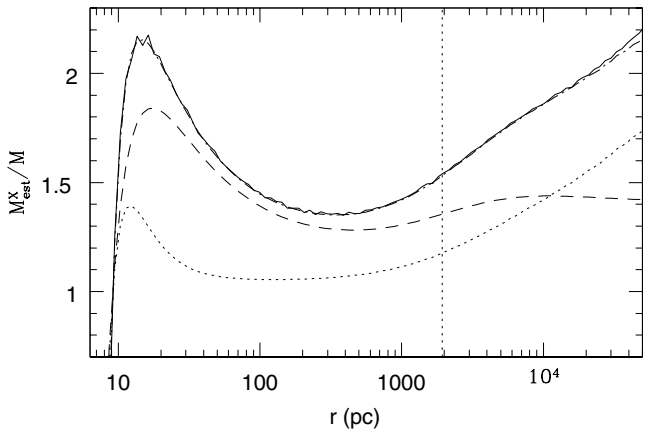

Figure 2. The radial trend of $M^{\rm X}_{\rm est}/M$ obtained from equation (7), for the partial wind model described in Section 3.3.1 (solid line). Also shown are the terms on the right-hand side of equation (8): the radial derivative term (plus unity, dotted line), the term with the mass source (plus unity, dashed line), and $M^{\rm X}_{\rm est}/M$ according to equation (8) (dot–dashed line). The dotted vertical line marks the position of $R_{\rm e}$.

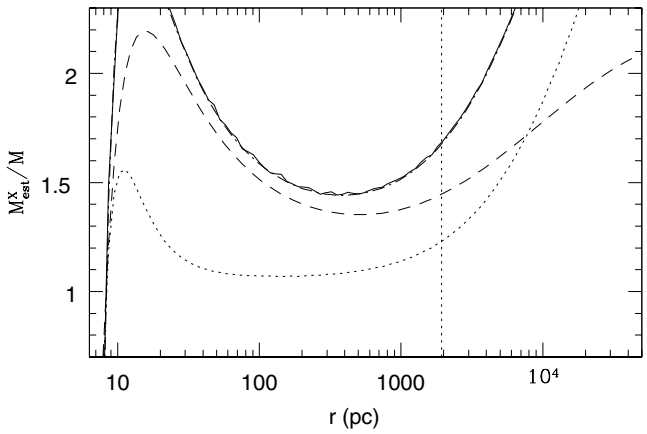

Figure 3. The same as in Fig. 2, for a model with a larger fraction of dark matter content within $R_{\rm e}$ [$(M_{\rm h}/M_*)_{\rm e} = 1.3$], consistent with the X-ray analysis of F06 (see Section 3.3.2). Again $\vartheta = 0.72$ and $s = 1.1$.

NGC 3379, the hot ISM luminosity in the 0.2–5 keV band is less than that derived by F06 by at least an order of magnitude. If the SN Ia rate is lowered, the hot gas flow maintains in a wind phase over most of the galactic body, while it develops an inflow in a very small central region ($\lesssim$20 pc; see the partial wind case in Fig. 1). In this way, a higher luminosity is obtained at the present epoch, that is comparable to the observed one when ϑ is close to its lowest values ($\vartheta \sim 0.7$).

In Fig. 2, the derived $M^{\rm X}_{\rm est}/M$ is shown for a sample case of a partial wind with a hot gas luminosity of $L(0.2\text{–}5\,{\rm keV}) = 3.6 \times 10^{37}$ erg s^{-1} and an emission-weighted temperature of 0.53 keV, both values close to those reported by F06 (see Table 1).[3] It is obtained for $s = 1.1$ and $\vartheta = 0.72$, after a time of 8 Gyr. $M^{\rm X}_{\rm est}(r)$ overestimates $M(r)$, by a factor of $\sim$1.5–1.6 around $R_{\rm e}$. This factor is in the direction of, and also enough for, the explanation for the residual discrepancy between $M^{\rm X}_{\rm est}$ derived by F06 and the total mass derived with optical methods (Section 2.2). Note how the $M^{\rm X}_{\rm est}/M$ profiles derived with equations (7) and (8) maintain remarkably close to each other over the whole numerical grid. This means that the terms describing the deviation from hydrostatic equilibrium and entering equation (8) are really accounting for the whole discrepancy measured with equation (7) (and it is also an independent check of the reliability and accuracy of the numerical code).

3.3.2 X-ray derived and maximum dark mass model

We study here a galaxy model with $(M_{\rm h}/M_*)_{\rm e} = 1.3$, in accordance with the $M^{\rm X}_{\rm est}$ derived by F06 (Section 2.2); the global $M_{\rm h}/M_* = 1.5$ as in Section 3.3.1, and the SN Ia parameters are varied.

Again, for $\vartheta = 1$ global winds that are far less luminous than the observed $L_{\rm X}$ are obtained, when the galaxy is 9 Gyr old. Luminosity and temperature close to the observed values are shown again when the flow is a partial wind, with approximately the same low SN Ia rates derived in the previous section ($\vartheta \sim 0.7$). This fact can be explained by considering that, although $(M_{\rm h}/M_*)_{\rm e}$ increases from 0.13 to 1.3, the total mass in the central region remains the same, and the absolute value of the binding energy per unit mass decreases by $\sim$15 per cent at the centre; this is the outcome of imposing fixed values for the central stellar velocity dispersion and $R_{\rm e}$ (see equations 5 and 6). In addition, being L_B also fixed, the rates of mass and heat input are the same as in the set of models of Section 3.3.1. All in all, the net result is just a small reduction of the binding energy in the central region, where almost all of the emission is produced.

Since the flow pattern is the same as in the previous section, also the mass estimates $M^{\rm X}_{\rm est}$ suffer from the same problems. Fig. 3 shows such an estimate for a model with $L_{\rm X} = 2.5 \times 10^{37}$ erg s^{-1} and a temperature of 0.53 keV, after 8 Gyr; the input SN Ia parameters are $s = 1.1$ and $\vartheta = 0.72$. While similar to Fig. 2 in the general trends of the various quantities, the overestimate is even larger than that in Fig. 2. Thus, even if $(M_{\rm h}/M_*)_{\rm e}$ were really as high as deduced from assuming hydrostatic equilibrium, the derived $M^{\rm X}_{\rm est}$ would be wrong. This experiment also shows that the hot ISM is quite insensitive to the underlying mass distribution and partition between stellar and dark mass within $R_{\rm e}$, at least for these low dark matter contents.

In the last experiment, we check whether reliable mass estimates can ever be obtained with the X-ray procedure of equation (1), for this galaxy. This requires the hot gas to be roughly in hydrostatic equilibrium over most of the galaxy, as in a slow global inflow (e.g. Ciotti et al. 1991). In order to obtain an inflow over a large region, the dark matter content must be increased. Therefore, we assume the maximum dark matter content allowed for by optical studies (Saglia et al. 1992), that is, a global ratio of $M_{\rm h}/M_* = 5$ and $(M_{\rm h}/M_*)_{\rm e} = 0.83$ (note that this latter value is also consistent with the estimate of F06, within the uncertainties; see Section 2.2). If $\vartheta \sim 0.7$, the galaxy indeed hosts a global inflow; however, after an ageof 9 Gyr, it is far more luminous than observed ($L_{\rm X} \gtrsim 10^{40}$ erg s^{-1}). For $\vartheta > 0.7$, the flow pattern is again a global inflow during the first part of the evolution, but before reaching an age of 9 Gyr, it slows down until it reverts its direction into an outflow, over most of the galaxy. The final phase is a partial wind, whose luminosity is much lower than that in a model where the gas is still mostly inflowing. For example, if $\vartheta = 0.92$ and $s = 1.0$, the transition epoch is at $\sim$9 Gyr, after which the luminosity decreases by two orders of magnitude in $\lesssim$1 Gyr. The observed L(0.2–5 keV) is reached between 10 and 10.5 Gyr, with an average emission temperature of $\sim$0.4 keV. Fig. 4 shows the mass profile that would be derived for this model: as for the previous cases, an overestimate is obtained

[3] A contribution from unresolved sources to L(0.2–5 keV) in Table 1 (Section 2.2), and the uncertainty associated with this measurement, can account for the slightly lower $L(0.2\text{–}5\,{\rm keV})$ of the model.

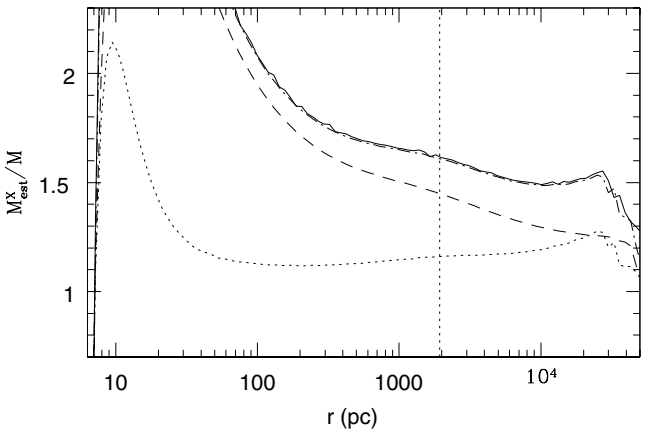

Figure 4. The same as in Figs 2 and 3, for the maximum dark mass model, where an inflow reverts into a partial wind (PW) at ∼9 Gyr (see Section 3.3.2).

at R_e. This experiment shows that the X-ray procedure applied to NGC 3379 is forced to produce mass overestimates, because the low observed X-ray emission requires that the gas is outflowing over most of the galaxy.

4 CONCLUSIONS

We have analysed the discrepancy between optical and X-ray mass estimates of NGC 3379, a well-studied nearby elliptical for which optical investigations are consistent even with the absence of dark matter, but for which recent X-ray studies derived a total mass much larger than that derived with optical methods, within R_e. First, we have reduced the discrepancy to a more plausible factor of ∼2, by a reanalysis of the total mass within R_e implied by previous optical studies. Then, we have argued in favour of the hypothesis of lack of hydrostatic equilibrium as the explanation for the residual inconsistency between the X-ray and optically derived total mass.

With the aid of hydrodynamical simulations tailored specifically for NGC 3379, we have tested whether hot gas properties similar to those observed can be recovered, and then what total mass is derived if the standard X-ray procedure is applied to the flow resulting from the simulation. In a first experiment, the total mass distribution underlying the gas flow is that derived by the modelling of the optical data, with $(M_h/M_*)_e = 0.13$. For an SN Ia explosion rate consistent with current estimates, a hot gas flow with luminosity and temperature close to the *Chandra* values can be obtained. However, except for a very small central region, the gas is largely outflowing, with a velocity increasing outwards. For such a flow, the X-ray method based on the hypothesis of hydrostatic equilibrium gives an overestimate of the total mass by a factor of ∼1.6, within R_e, and by $\gtrsim$2 at larger radii.

In a second experiment, the underlying total mass distribution is that derived by the modelling of the X-ray data within R_e, under the assumption of hydrostatic equilibrium; that is, $(M_h/M_*)_e$ is increased to 1.3, while the global M_h/M_* is the same as before. Again, the observed hot gas properties are reproduced by a partial wind; therefore, the assumption of hydrostatic equilibrium and the use of the X-ray method produce a mass overestimate of a similar factor, showing the inconsistency of the whole procedure for this galaxy. This experiment also shows that the hot ISM is quite insensitive to the underlying distribution of dark mass within R_e, at least for these low dark matter contents.

Finally, we have tried a 'maximum' dark matter model, where the amount of dark mass is the maximum allowed for by optical studies [$M_h/M_* = 5$ and $(M_h/M_*)_e = 0.83$, which is also consistent with the X-ray results]. The flow can now keep itself in a global inflow, the gas is close to hydrostatic equilibrium over most of the galaxy, and the galaxy mass estimated with the X-ray method would be reliable, but the X-ray luminosity is orders of magnitude higher than that observed. A luminosity as low as that observed is obtained if the SN Ia rate is increased, so that the flow starts as a global inflow and becomes a partial wind in later times. Therefore, the X-ray method again produces an overestimate of the total mass at R_e.

In conclusion, NGC 3379 is a clear example where the departure from hydrostatic equilibrium of the hot ISM gives a consistent explanation for the discrepancy between the optical and X-ray-derived mass values. In particular, this departure (while also required to reproduce the observed low X-ray emission) accounts for M^X_{est} being an overestimate and also for the *size* of the overestimate. This analysis suggests that a previous understanding of the hot gas behaviour is required before attempting dynamical estimates with hot gas-based studies. Here, for example, the very low hot gas content suggests by itself that most of the galaxy likely hosts a wind.

Lastly, we can check whether the X-ray properties of NGC 3379 can put any constraint in the controversy concerning the 'dearth of dark matter in elliptical galaxies', for which NGC 3379 has been suggested to provide an example (e.g. Romanowsky et al. 2003), later criticized by Dekel et al. (2005). We find that hot gas with an emission and average temperature as observed by *Chandra* can be present for the whole range of dark mass amount and distribution suggested by optical works, just varying the SN Ia rate within its estimated uncertainty (i.e. it has to be not so high to sustain a global wind, for the lowest M_h/M_* values, and not so low that a global inflow lasts until the present epoch, for higher M_h/M_* up to 5). Even higher dark matter contents than those found by optical works can actually still correspond to partial winds with the required X-ray properties. This insensitiveness to the underlying mass is not totally new: although for much X-ray brighter galaxies, mass models constrained by extended stellar dynamical data, and including different amounts of dark matter, were found to produce similar temperature and X-ray brightness profiles, within the uncertainties in the X-ray measurements (Bertin, Pignatelli & Saglia 1993). The situation may have improved with the *Chandra* and *XMM–Newton* data, at least for the X-ray brightest galaxies.

ACKNOWLEDGMENTS

We thank the anonymous referee for comments that improved this presentation. We acknowledge support from MIUR (Cofin 2004) and from contract ASI-INAF I/023/05/0.

REFERENCES

Bertin G., Pignatelli E., Saglia R. P., 1993, A&A, 271, 381
Bertin G. et al., 1994, A&A, 292, 381
Brown B. A., Bregman J. N., 2001, ApJ, 547, 154
Capaccioli M., Held E. V., Lorenz H., Vietri M., 1990, AJ, 99, 1813
Cappellaro E., Evans R., Turatto M., 1999, A&A, 351, 459
Cappellari M. et al., 2006, MNRAS, 366, 1126
Ciardullo R., Jacoby G. H., Dejonghe H. B., 1993, ApJ, 414, 454
Ciotti L., 1996, ApJ, 471, 68
Ciotti L., Pellegrini S., 1992, MNRAS, 255, 561
Ciotti L., Pellegrini S., 2004, MNRAS, 350, 609 (CP04)
Ciotti L., D'Ercole A., Pellegrini S., Renzini A., 1991, ApJ, 376, 380

Dekel A., Stoehr F., Mamon G. A., Cox T. J., Novak G. S., Primack J. R., 2005, Nat, 437, 707
de Vaucouleurs G., 1948, Ann. Ap., 11, 247
Dubinski J., Carlberg R. G., 1991, ApJ, 378, 496
Evans N. W., Collett J. L., 1997, ApJ, 480, L103
Fabbiano G., 1989, ARA&A, 27, 87
Fabricant D., Lecar M., Gorenstein P., 1980, ApJ, 241, 552
Fukazawa Y., Botoya-Nonesa J. G., Pu J., Ohto A., Kawano N., 2006, ApJ, 636, 698 (F06)
Gerhard O., Kronawitter A., Saglia R. P., Bender R., 2001, AJ, 121, 1936
Greggio L., 2005, A&A, 441, 1055
Halliday C., Davies R. L., Kuntschner H., Birkinshaw M., Bender R., Saglia R. P., 2001, MNRAS, 326, 473
Hernquist L. E., 1990, ApJ, 536, 359
Kronawitter A., Saglia R. P., Gerhard O., Bender R., 2000, A&AS, 144, 53
Maraston C., 2005, MNRAS, 362, 799
Navarro J. F., Frenk C. S., White S. D. M., 1996, ApJ, 462, 563
Pellegrini S., 2005, MNRAS, 364, 169
Pellegrini S., Ciotti L., 1998, A&A, 333, 433
Peletier R. F., Davies R. L., Illingworth G., Davis L. E., Cawson M., 1990, AJ, 100, 1091
Pierce M. et al., 2006, MNRAS, 366, 1253
Renzini A., Ciotti L., 1993, ApJ, 416, L49
Romanowsky A. J., Douglas N. G., Arnaboldi M., Kuijken K., Merrifield M. R., Napolitano N. R., Capaccioli M., Freeman K. C., 2003, Sci, 301, 1696
Saglia R. P., Bertin G., Stiavelli M., 1992, ApJ, 384, 433
Samurovic S., Danziger I. J., 2005, MNRAS, 363, 769
Schweizer F., Seitzer P., 1992, AJ, 104, 1039
Sun M., Forman W., Vikhlinin A., Hornstrup A., Jones C., Murray S. S., 2003, ApJ, 598, 250
Teodorescu A. M., Mendez R. H., Saglia R. P., Riffeser A., Kudritzki R.-P., Gerhard O. E., Kleyna J., 2005, ApJ, 635, 290
Terlevich A. I., Forbes D. A., 2002, MNRAS, 330, 547
Tonry J. L., 1983, ApJ, 266, 58
Tonry J. L., Dressler A., Blakeslee J. P., Ajhar E. A., Fletcher A. B., Luppino G. A., Metzger M. R., Moore C. B., 2001, ApJ, 546, 681
Trinchieri G., Pellegrini S., Wolter A., Fabbiano G., Fiore F., 2000, A&A, 364, 53
Tsai J. C., 1994, ApJ, 429, 119
White D. A., Jones C., Forman W., 1997, MNRAS 292, 419

This paper has been typeset from a TEX/LATEX file prepared by the author.